3D heat transfer model of hybrid laser Nd:Yag-MAG welding of S355 steel and experimental validation

Emilie Le Guen [a], Muriel Carin [b,*], Rémy Fabbro [a], Frédéric Coste [a], Philippe Le Masson [b]

[a] PIMM, Arts et Métiers ParisTech, 151, boulevard de l'Hôpital, 75013 Paris, France
[b] LIMATB, Université de Bretagne-Sud/UEB, Centre de recherche C. Huygens, Rue de Saint Maudé, BP 92116, 56321 Lorient Cedex, France

A B S T R A C T

A three-dimensional heat transfer model was developed to predict the temperature fields, the weld geometry and the shape of the solidified weld reinforcement surface during hybrid laser-MAG arc welding of fillet joints. Melt pool deformation due to arc pressure was calculated by minimizing the total surface energy. A series of hybrid welding experiments was conducted on S355 steel for different welding speeds and wire feeding rates. A high speed video camera was used to measure weld pool depression and surface weld pool geometry. Visualization of the weld pool during welding has also allowed for a better understanding of the interaction between the keyhole and droplets. The various weld bead shapes were explained through these observations. The arc pressure, the surface energy distribution, and arc efficiency were evaluated by comparing experimental data and numerical results for a wide range of welding operating parameters. Good correlation was found between the calculated and experimental weld bead shapes obtained for the hybrid laser-MAG arc welding process as well as for laser or MAG alone.

1. Introduction

Gas metal arc welding, also called GMA or GMAW, is a general term for the MIG or MAG welding processes and is characterized by a consumable wire electrode. During MIG welding (metal inert gas), an inert gas such argon or helium is used as a shielding gas, whereas in MAG welding (metal active gas), an active gas such as CO_2 or O_2 is employed. To improve the gas metal arc welding performance, one of the most promising alternatives is laser hybrid welding. This process, combining laser keyhole welding with an electric arc, has been known since the 1970s, but has only recently begun to be used in industrial applications. Deep penetration allows for the welding of rather thick materials even at high welding speeds allowing for the filling of unavoidable gaps of the joints, with possible improved metallurgical properties and controlled geometry of the weld seam [1,2]. Although there is a growing interest in this process, the thermal cycles induced by the combination of these two welding processes are still not well known. The precise knowledge of temperature history is essential for predicting accurately the distortions and weld residual stresses. It is known that the strength of a weld seam is controlled by many parameters. Its geometry is one of these crucial parameters that have to be controlled or even optimized if one wants to minimize the effect of an induced stress field generated during the loading cycles of these welds. Similarly the metallurgical properties of these welds also depend on the thermal cycles induced by the involved heat sources, the arc and the laser, which are used during this process [3]. So far, most of the hybrid laser-MIG/MAG welding research focuses on how to effectively combine a laser welding process with an arc welding process together using experimental methods. These works consist in studying the influence of various operating parameters on the weld joint shapes [4–6]. It should be mentioned that most of these works are essentially based on macrograph analysis. However, observations with a high speed video camera can give insight on the physical phenomena and help in understanding the interaction between the many parameters involved in this process. For example, Fabbro et al. have shown the interest of using high speed video cameras for analyzing hydrodynamic regimes during laser welding [7].

In addition, there is very limited amount of research which focuses on modeling the hybrid laser-MAG welding process. This process is rather complex and there is no available complete understanding of it that is satisfactory. We know that each process alone is not already completely mastered or understood, nor is their combination. Therefore, the development of a mathematical modeling of this hybrid process that would take into account the main involved physical processes would be a very useful tool for estimating the final parameters of the weld seam for a given set of operating parameters. We can mention the work done by Wouters, who has developed a semi-analytical model to calculate the temperature field and melt pool shape during hybrid laser-MIG welding [8].

Nomenclature

c_p^{eq}	equivalent specific heat (J kg^{-1} K^{-1})
d	distance between laser beam and arc (m)
g	gravitational constant (m s^{-2})
h	convective heat transfer coefficient (W m^{-2} K^{-1})
H_{cyl}	height of the cylinder (m)
I	current (A)
k_{eff}	enhanced thermal conductivity (W m^{-1} K^{-1})
L_f	latent heat of fusion (J kg^{-1})
$\vec{n}$	unit external normal vector
P_{arc}	arc power (W)
P_{surf}	surface pressure (Pa)
P_{max}	maximum arc pressure (Pa)
r_q	heat distribution parameter (m)
r_w	wire radius (m)
T	temperature (K)
T_0	ambient temperature (K)
T_m	melting temperature (K)
ΔT	difference between liquidus and solidus (K)
U	voltage (V)
U_0	welding speed (m s^{-1})
U_w	wire feeding rate (m s^{-1})

Greek symbols

γ	surface tension (N m^{-1})
ε	emissivity
η	arc efficiency
λ	Lagrange multiplier
ρ	density (kg m^{-3})
σ	Stefan–Boltzmann constant (W m^{-2} K^{-4})
σ_p	arc pressure distribution parameter (m)
ϕ	vertical displacement of top surface (m)

Reutzel et al. have proposed a three-dimensional thermal finite element model using a volumetric double ellipsoidal heat source to represent both laser and GMA energy [9]. A similar approach was recently used by Zhang for the laser GMAW-P hybrid welding process [10]. In the aforementioned works, the initial geometry takes into account weld reinforcement which is assumed to be known and present before welding. Such an approach does not allow for the consideration of the energy deposit from the arc or laser which actually occurs on the deformed surface of the weld pool due to pressure effects. More sophisticated numerical models were proposed by Zhou and Tsai to investigate transport phenomena in hybrid laser-MIG welding [11]. It includes the calculation of the temperature field, pressure balance, melt flow, free surface evolution, laser-induced plasma formation and multiple reflections as a function of time. The volume of fluid (VOF) method is used to track the free surface. However, this model is limited to a two-dimensional axial-symmetric approach which does not represent a realistic assumption. The extension of such a model to a three-dimensional configuration was proposed by Cho to examine the complex flow patterns of the molten pool in GMA-laser hybrid welding, but no comparison with experimental data was done [12].

In this paper, a numerical model is developed to calculate the thermal cycles in S355 steel welded by the hybrid laser-MAG process for a given set of welding parameters. This model is able to predict the 3D geometry of the weld reinforcement observed at the top of welded samples and the deformation of the melt pool induced by the arc pressure and droplets. The calculation of the melt pool deformation is needed to define accurately the location where the arc energy is deposited onto the melt pool surface. The profile of the weld pool surface is calculated using a static energy minimization. The equation of energy is then solved in this deformed geometry. The heat source modeling the GMA process is applied on the deformed shape of the molten pool. Our goal here is to define a numerical tool that is rather easy to run and precise enough to determine the thermal cycles and the shapes of weld pool. To obtain very short computation time, the fluid flow in the melt pool was not considered. This model is then compatible with a future thermomechanical analysis of hybrid laser-MAG welding. A main difficulty in the numerical simulation of the welding process is the choice of the heat source parameters, since they are not directly measurable. In this study, these parameters are calibrated using numerous observable parameters deduced from high speed camera observations and macrographs. The numerical results are compared with corresponding experimental observations for a wide range of welding parameters.

2. Modeling hybrid laser/MAG process

2.1. Formulation

During the MAG process, metal is heated with an arc between a continuously fed filler metal electrode and the material to be welded. The arc is created by the voltage drop imposed between the contact tube and the workpiece. Shielding is obtained from an externally supplied active gas. The electrode wire is melted by internal resistive power and heat transferred from the arc. The melting of the electrode wire causes rapid formation of droplets at the wire tip. Droplets of molten metal are detached and transferred from the wire to the weld pool by a combination of gravitational, Lorentz, surface tension and plasma forces. Metal transfer can occur in three different modes: spray, globular, and short-circuiting. In globular and spray mode transfer, discrete metal droplets travel across the arc gap. The droplet size in spray transfer is smaller than in globular transfer. In short-circuiting transfer, the molten metal in the wire tip is transferred to the molten pool when the wire touches the surface of the pool. The mode of transfer is determined by the heat input and the type of shielding gas used. In general, the short-circuiting transfer occurs between 100 and 200 A, the globular mode between 200 and 250 A and the spray mode between 250 and 400 A. In the present study, the three transfer modes will be observed as the current values used range from 146 to 365 A, confirmed by high speed camera observation. The weld pool surface is deformed by forces exerted by the arc and droplets. This depression increases with arc current [13]. In laser welding, the heat required for welding is produced by a focused laser beam. The high power density laser beam induces strong evaporation at the melt surface. The vaporization recoil pressure is sufficient to produce a deep, narrow depression in the molten material, called a keyhole.

While combining these two processes, laser and GMA, the laser and the arc act simultaneously in a unique weld pool in which the keyhole and the droplets can interact. Fig. 1a illustrates the principle of the laser-MIG/MAG hybrid welding process. During a trailing torch arc, as in Fig. 1a, the torch follows the laser beam in the welding direction. The inverse arrangement is called a leading torch position (Fig. 1b).

This study mainly concerns the prediction of the weld geometry so that only thermal conduction phenomena are taken into account. In GMAW, the heat entering the melt pool comes from the energy produced by resistive heating inside the plasma and the enthalpy of molten droplets transferring from the welding wire. Since

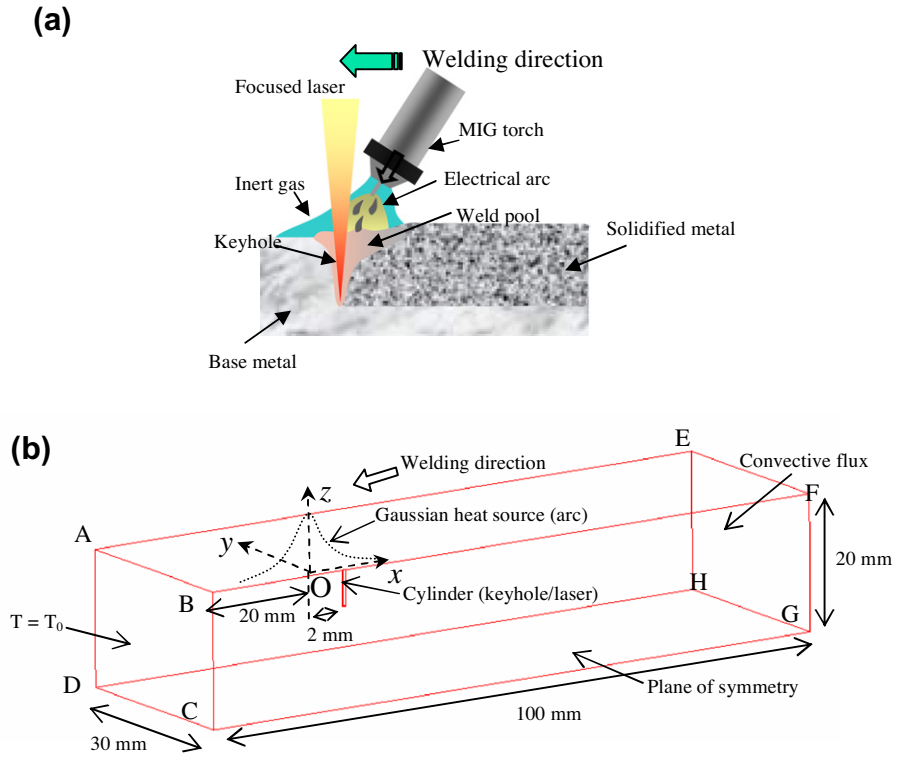

Fig. 1. Schematic sketch of laser-MIG/MAG hybrid welding process (a) and computational domain size (b).

resistive heating which occurs in the melt pool is negligible [14], the energy from the plasma is essentially transferred at the surface of the melt pool. The heat input from molten droplets can be modeled by a surface or volume heat source. Xu and Wu recommend a volume heat source for welding currents higher than 260 A [15]. In which case, additional unknown parameters are required, such as the height and the diameter of the volume heat source. In the present study, to limit the number of unknown parameters, the heat source associated to the arc and the droplets is modeled by a unique surface heat source for all currents. For the same reason, this heat source is assumed to have a Gaussian distribution symmetric around the z-axis, as it is commonly used in GMAW modeling (Fig. 1b). However, the numerical works done by Xu et al. have shown that the distributions of the heat flux, arc pressure, and current density on the workpiece surface were not really Gaussian due to the presence of droplets [16]. The heat source generated by the laser beam is represented by a moving cylinder with a uniform temperature along its wall. The wall temperature is considered equal to the boiling point, as is commonly assumed [17]. The laser power is supposed to be completely absorbed by the wall of the keyhole. The height of the cylinder is equal to the depth of the keyhole and is given by the following empirical law:

$$H_{cyl}(U_0, P_{arc}) = 0.14U_0^2 - 0.078U_0P_{arc} - 1.45U_0 - 0.0079P_{arc}^2 + 0.52P_{arc} + 5.45 \quad (1)$$

where H_{cyl} (mm) is the height of the cylinder, U_0 (m/min) is the welding velocity and P_{arc} (kW) is the arc power $U\,I$. The coefficients were determined using the function polyfitn of Matlab and a large number of macrographs obtained in hybrid laser/MAG [18]. The best fit between the calculated and measured depths of the fusion zone is obtained when the height of the cylinder in the model is lower than the depth of the weld joint by a factor of 0.2 mm. The error between the calculated and measured values is less than 7%.

It is worth noting that this empirical law depends on our welding conditions and material. The diameter of the keyhole is supposed to be equal to the diameter of the laser spot at the focus point (here 0.6 mm), which correlates well with experiments. It should be mentioned that the welding velocities used in experiments in the range of 0.5–4 m/min are sufficiently low to assume a co-axial keyhole with laser beam [7]. The other assumptions of this model are:

1. Quasi-steady-state conditions: the heat equation is then written in a moving coordinate system which moves at the same velocity as the heat source.
2. Material properties are temperature-dependent except for the liquid phase and taken from OTUA [19]. The filler material is supposed to have the same properties as S355 steel. The thermal properties are first tabulated and then interpolated using a piecewise cubic method.
3. The latent heat of fusion is taken into account using the apparent heat capacity formulation.
4. Fluid flow in the weld pool is not considered, but thermal conductivity of the liquid phase is enhanced to account for convective heat transfer in the weld pool. This method has been largely used in the past to simulate laser welding [20,21], or GMA welding [22,23] with a purely conductive model. When convection occurs in the melt pool, thermal transport is accelerated by fluid flow and the isotherms are modified in the direction of the flow. An easy way to reproduce this effect using a conductive model is to assign the material an artificially isotropic or anisotropic high thermal conductivity in this area.
5. Metallurgical phenomena are not taken into consideration. The values of the latent heat of the metallurgical phase change are generally small compared to solid–liquid latent heat.
6. The pool surface is assumed to be in a static equilibrium with respect to arc pressure, gravity and surface tension. The effect of fluid flow induced by Marangoni phenomena or electromagnetic forces is ignored.

2.2. Governing equations

A three-dimensional Cartesian coordinate is used in the calculation, while only half of the workpiece is considered since the weld is symmetrical about the weld centerline. The dimensions of the computational domain are indicated in Fig. 1b. The width and length are smaller than the size of the sample to reduce computation time. These dimensions were chosen so as to have no influence on the calculated size of the melt pool. The keyhole can be located at a distance ±d from the arc depending on the trailing or leading configuration. By using a coordinate system attached with the heat source, the following energy conservation equation can be written in the Cartesian coordinate system:

$$\rho c_p^{eq} U_0 \frac{\partial T}{\partial x} = \frac{\partial}{\partial x}\left(k_{eff}\frac{\partial T}{\partial x}\right) + \frac{\partial}{\partial y}\left(k_{eff}\frac{\partial T}{\partial y}\right) + \frac{\partial}{\partial z}\left(k_{eff}\frac{\partial T}{\partial z}\right) \tag{2}$$

where ρ is the density, c_p^{eq} is an equivalent specific heat capacity which includes the latent heat of fusion, k_{eff} is the enhanced thermal conductivity, U_0 is the welding speed of the heat source moving along x-axis, T is the temperature and x, y, z represent the coordinates in the deformed mesh. The values of density, heat capacity, and thermal conductivity are taken from [19] for the solid phase and equal to 7290 kg m^{-3}, 707 J kg^{-1} K^{-1} and 32 W m^{-1} K^{-1}, respectively for the liquid phase. The value of the liquid thermal conductivity is multiplied by a factor of enhancement given in Table 1. These values are discussed for each process in Section 4.3.

The equivalent heat capacity has the following expression:

$$c_p^{eq} = c_p + L_f \frac{\exp\left(-\frac{(T-T_m)^2}{\Delta T^2}\right)}{\sqrt{\pi \Delta T^2}} \tag{3}$$

where c_p is the specific heat capacity, L_f = 270,000 J kg^{-1} is the latent heat of fusion, T_m = 1745 K is the melting temperature and ΔT = 65 K is the difference between solidus and liquidus temperature.

2.3. Boundary conditions

The heat input from the arc, assumed to have a Gaussian distribution, is applied to the top of the workpiece (ABFE, Fig. 1b), which is expressed as follows:

$$k\nabla T \cdot \vec{n} = \frac{\eta UI}{2\pi r_q^2}\exp\left(-\frac{x^2+y^2}{2r_q^2}\right) - \varepsilon\sigma(T^4 - T_0^4) - h(T - T_0) \tag{4}$$

where $\vec{n}$ is the external unit vector, normal to the top surface, η is the arc power efficiency, U is the welding voltage, I is the welding current, r_q is the heat distribution parameter, ε = 0.5 is the emissivity, σ is the Stefan–Boltzmann constant, T_0 = 293 K is the ambient temperature and h = 15 W m^{-2} K^{-1} is the convective heat transfer coefficient. The values for ε and h are mean values taken from the literature [24,25]. However, the model is not strongly influenced by these values since the heat losses from radiation and convection represent less than 15% of the heat source.

On the plane of symmetry (BCGF), a thermal insulation boundary condition is applied. The temperature at the front side (ABCD) is set to the ambient temperature. At the back side (EFGH), since the size of the computational domain along the x-axis is reduced, a convective flux is applied:

$$k\nabla T \cdot \vec{n} = -\rho c_p^{eq}(T - T_0)\vec{U_0}\cdot\vec{n} \tag{5}$$

For all other surfaces assumed to be surrounded by ambient air (ADEH, CDHG), heat losses from radiation and convection are considered with h = 15 W m^{-2} K^{-1} and ε = 0.5.

Table 1
Enhancement factors of the liquid thermal conductivity for each process.

Laser	Anisotropic along x-axis: ×6	
	2 m/min < U_w < 7 m/min	7 m/min < U_w < 12 m/min
MAG	Isotropic: ×1	Isotropic: ×3
Hybrid	Anisotropic along x-axis: ×6	Isotropic: ×3

2.4. Surface deformation

Depending on the arc current and voltage, the weld pool surface can exhibit significant deformation below the arc followed by weld reinforcement due to the melting of filler wire. In that case, the weld pool surface has a shape that must satisfy, at steady state, an equilibrium condition between surface tension, hydrostatic pressure, and arc pressure. Ushio and Wu have previously proposed a solution for this problem to predict the weld pool geometry in gas metal arc welding [13]. This work is based on a variational approach that minimizes the total energy of the melt pool, with the constraints that the melt pool has a constant volume and weld reinforcement geometry is defined by the filler wire mass flow. The energy of the melt pool taken into account concerns the variation of surface energy with a corresponding change of its area, the total potential energy inside the gravitational field, and the work performed during that change of area by the arc pressure and droplet flow momentum. We have adapted this approach to predict the weld pool deformation in hybrid laser-MAG welding. The model was developed using Comsol Multiphysics® software.

In the case of gas–metal arc welding, the total energy to be minimized includes the surface energy, the potential energy due to gravity, and the work performed by the arc pressure and the droplet impact displacing the pool surface. The total energy can, therefore, be expressed as:

$$\begin{aligned} E_t &= \iint_s \left(\gamma\left(\sqrt{1+\phi_x^2+\phi_y^2}-1\right) + \frac{1}{2}\rho g\phi^2 - P_{surf}\phi\right)dx\,dy \\ &= \iint_s F\,dx\,dy \end{aligned} \tag{6}$$

where s means the top surface of the workpiece, γ = 1 N m^{-1} is the surface tension of the molten metal, ρ = 7290 kg m^{-3} is the density of the molten metal, P_{surf} is the pressure due to arc and droplets. To reduce the number of unknown parameters, the pressure due to the impact of the droplets and arc pressure were gathered in a unique term. ϕ is the space function representing the weld pool deformation, or in other words the vertical displacement of the top surface. Here ϕ is positive for a downward movement. The subscripts x and y refer to the derivative with respect to x and y, respectively.

Since the deposited area at a solidified cross section of the fillet weld is equal to the amount of fed wire per unit length, the constraining equation is given as:

$$\iint_s -\phi\,dx\,dy = \iint_s G\,dx\,dy = \Delta V_d \tag{7}$$

where ΔV_d represents the additional volume due to the feed wire in MAG welding.

If one applies the Euler–Lagrange criterion,

$$\frac{\partial}{\partial\phi}(F+\lambda G) - \frac{\partial}{\partial x}\left[\frac{\partial}{\partial\phi_x}(F+\lambda G)\right] - \frac{\partial}{\partial y}\left[\frac{\partial}{\partial\phi_y}(F+\lambda G)\right] = 0 \tag{8}$$

where λ is the Lagrange multiplier.

Since

$$\frac{\partial}{\partial\phi}(F+\lambda G) = \rho g\phi - P_{surf} - \lambda \tag{9}$$

and

$$\frac{\partial}{\partial \phi_x}(F+\lambda G)=\gamma\frac{\phi_x}{\sqrt{1+\phi_x^2+\phi_y^2}} \tag{10}$$

and

$$\frac{\partial}{\partial \phi_y}(F+\lambda G)=\gamma\frac{\phi_y}{\sqrt{1+\phi_x^2+\phi_y^2}} \tag{11}$$

by substituting Eqs. (9)–(11) in Eq. (8), it follows that:

$$-\frac{\partial}{\partial x}\left(\gamma\frac{\phi_x}{\sqrt{1+\phi_x^2+\phi_y^2}}\right)-\frac{\partial}{\partial y}\left(\gamma\frac{\phi_y}{\sqrt{1+\phi_x^2+\phi_y^2}}\right)+\rho g\phi = P_{surf}+\lambda \tag{12}$$

The pressure applied on the melt pool surface is assumed as the following Gaussian distribution:

$$P_{surf}=P_{max}\exp\left(-\frac{x^2+y^2}{2\sigma_p^2}\right) \tag{13}$$

where P_{max} is the maximum pressure and σ_p is the pressure distribution parameter. In the absence of literature data available for the MAG welding process, the value of P_{max} was calibrated based on the observed depression of the pool surface and the parameter σ_p was assumed to be equal to r_q. This assumption is based on the fact that the current distribution and the heat distribution are similar since most of the heat is carried by the electrons. This was confirmed by the measurements made by Tsai and Eager in GTA [26].

The boundary conditions for Eq. (12) are given as:

$$\text{At the front pool boundary}: \ \phi=0 \tag{14}$$

$$\text{At the rear pool boundary}: \ \frac{\partial\phi}{\partial x}=0 \tag{15}$$

2.5. Numerical method

The model presented here was developed using Comsol Multiphysics®. This software uses the finite element method to solve partial differential equations governing various physics and engineering problems. An attractive feature of this software is its ability to solve coupled equations in a moving mesh. The calculation of heat transfer with deformable weld pool surface was performed using the moving mesh capabilities in the Arbitrary–Lagrangian–Eulerian formulation (ALE) of this software. This model includes a 2D model to solve Eq. (12) and a 3D heat conductive model defined in the moving mesh (ALE) application mode to solve Eq. (2). To implement Eq. (12) in Comsol Multiphysics®, the 2D Helmholtz equation is chosen. It should be mentioned that the value of the Lagrange multiplier is automatically calculated. Indeed, with Comsol, it is easy to add a global constraint to a model. In our problem, the Lagrange multiplier is associated to the constraining mass conservation equation (Eq. (7)) which is expressed as follows:

$$\int -\phi_s dy=\frac{\pi r_w^2 U_w}{U_0} \tag{16}$$

where ϕ_s is the solidified surface profile and r_w, U_w, U_0 are the wire radius, wire feeding rate, and welding speed respectively.

Once the problem of surface deformation is solved, a 3D volume is created in which the top surface coincides with the deformed profile. This step is easily implemented in Comsol Multiphysics® using the moving mesh (ALE) application mode. The displacement of nodes located at the top surface is prescribed to the value of ϕ. The energy equation is then solved on this deformed mesh. It should be noticed that the deformation of the free surface is allowed only inside the melt pool. To ensure this condition, we used a high surface tension when temperature is lower than the melting point (γ = 40,000 N m^{-1}).

The main steps used in the algorithm are listed below:

(1) For an initially given isotherm at melting temperature, the deformed profile of the melt pool inside this isotherm is computed using the previous variational method.
(2) A 3-D volume is then created in which the top surface coincides with the deformed profile calculated in step 1.
(3) The thermal field is computed on this 3D volume.
(4) The resulting isotherm at melting temperature is then compared with the one used in step 1, and the entire process is repeated until convergence is obtained.

To enhance the accuracy of calculations, grids of variable spacing were employed consisting in around 25,000 elements for the 3D geometry and 16000 elements for the 2D geometry. The grid spacing is finer near the location of the heat source and coarser away from it. The minimum grid spaces were 300 μm for both 3D and 2D models. The workpiece size is 100 × 30 × 20 mm (length × ½ width × thickness). Due to the symmetry, only half of the workpiece was taken as the calculation domain, as previously mentioned. Fig. 2 shows a spatial convergence analysis

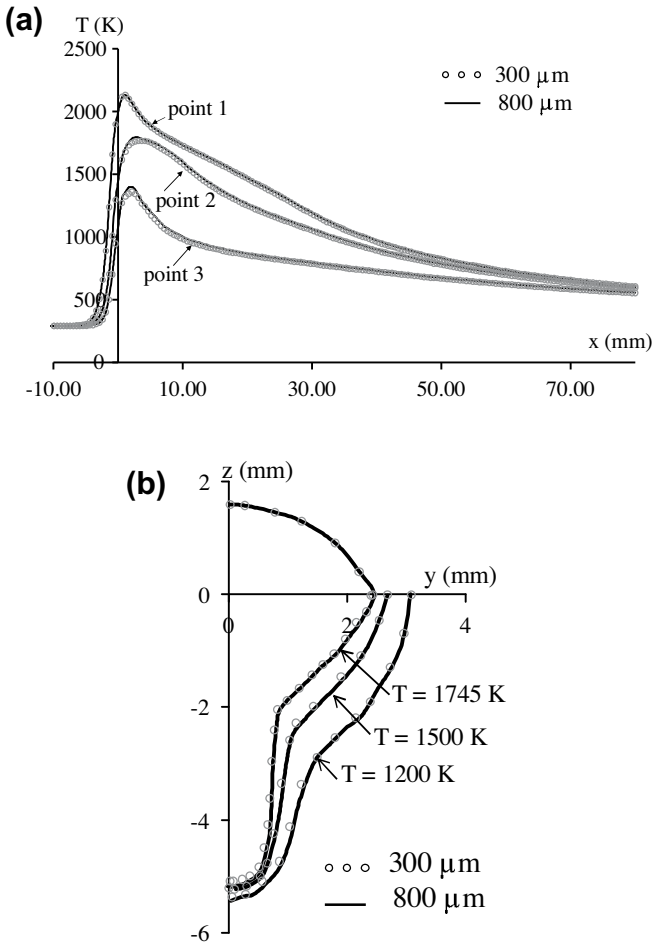

Fig. 2. Calculated thermal cycles at different positions (point 1: y = 2 mm, z = 0; point 2: y = 1 mm, z = −2 mm; point 3: y = 1 mm, z = −4.5 mm) and isotherms for two meshes (minimum grid space: 300 μm and 800 μm) in hybrid laser-MAG welding (model parameters: U = 17.6 V, I = 200 A, U_w = 5 m/min, U_0 = 1 m/min, η = 80, $r_q = \sigma_p$ = 1.5 mm, P_{max} = 900 Pa, k_{eff} = 192 W m^{-1} K^{-1}, H_{cyl} = 4.82 mm, d = 2 mm).

where the initial domain is discretized with two different meshes. Thermal cycles and isotherms correlate very well with the solution of the coarser mesh. The typical computer requirements were about 6 min on a notebook equipped with a two processor Intel Pentium 4 CPU 3.6 GHz and 3.5 Go RAM.

3. Experimental set-up

Experiments were carried out with a CW Nd:Yag Laser, with a constant power of 4 kW. The arc torch was a DIGI WAVE 400 model from SAFT PRO (Air Liquide Welding France). It delivers up to 400 A current for different configurations of control of current and tension of the arc. A standard mixture of shielding gas, namely Arcal21 (92% Ar and 8% of CO_2) flowing at 20 L/min was used, which justifies the term MAG in our case. In the present study, the laser beam was located at 2 mm from the arc torch with arc preceding laser. The vertical laser beam and the arc torch, having an inclination of 60° from the workpiece were fixed during experiments. The specimen mounted on a carriage was moved at various constant speeds. The bead-on-plate welding was performed using S355 structural steel with the following composition: 1.1% Mn, 0.003% Si, 0.014% P, 0.004% S, 0.03% Cu, 0.076% C, and 0.005% N. A G4Si1 filler material was used having a 1.2 mm diameter and the following composition: 1.5% Mn, 1% Si, 0.1% C.

The dynamics of the melt pool was analyzed with a CMOS fast camera (PHOTRON IMAGER FASTCAM APX RS 3000) with a recording rate of 10 kHz. The video images were processed to measure some relevant quantities for model validation, such as width and length of the surface weld pool, maximum deformation of the weld pool surface, droplet size and velocity. It also helps to understand the interaction between the keyhole and arc with droplets. To estimate the maximum surface deformation, from the video, we identify the deepest point of the melt pool surface, which is assumed to be vertical of the welding line, as shown in Fig. 3. It is worth noting that this point is more easily located from the video than from a fixed image. In this figure, the position of the keyhole is also indicated. The uncertainty in the measurement from high speed images was estimated at around 0.3 mm. To measure the longitudinal weld bead shape, an original method was developed. It consists in the insertion of a small cylinder made of aluminum–copper alloy along the weld centerline before welding. The specimen is then cut longitudinally along the weld centerline after welding. The contour between aluminum–copper alloy and steel is supposed to represent the solidification front. Further details about our experimental set-up can be found in [18,27].

4. Results and discussion

The model presented here needs the values of four unknown parameters: the arc efficiency η, the heat distribution parameter r_q, the maximum arc pressure P_{max} and the enhanced thermal conductivity k_{eff} used in the liquid phase. All these values were evaluated by comparing the experimental data with numerical results. The values of η and r_q control the width and depth of the weld joint and were estimated using the macrographs. For example, an increase of 5% on η leads to an increase of 5% on the width and depth of the melt pool. An increase of 20% on r_q induces an increase of 10% on the width and depth of the melt pool. The value of P_{max} governs the maximal surface deformation and was evaluated using the images from the fast camera. An increase of 20% on P_{max} induces an increase of 70% on the maximal surface deformation, this parameter is therefore one of the most sensitive parameters. The arc distribution parameter σ_p which is assumed to be equal to the heat distribution parameter r_q also influences the maximal deformation. An increase of 25% on σ_p will induce an increase of 30% on the maximal deformation. The parameter k_{eff} mainly influences the length of the melt pool and was estimated using the measured length from videos (Table 1). Fig. 4 shows the algorithm used for the identification of the four parameters. These different values were obtained by manually modifying the values of the input parameters in the computations until numerical results match the measured values. However, inverse methods could be used to calculate automatically the optimized values of the unknown parameters. The uniqueness of these estimated parameters for a given melt pool shape was demonstrated in [18]. The values of P_{surf}, η and r_q used in our computations can be fitted with a polynomial law:

$$Y(U_0, P_{arc}) = a \cdot U_0^3 + b \cdot U_0^2 \cdot P_{arc} + c \cdot U_0^2 + d \cdot U_0 \cdot P_{arc}^2 + e \cdot U_0 \cdot P_{arc} + f \cdot U_0 + g \cdot P_{arc}^3 + h \cdot P_{arc}^2 + i \cdot P_{arc} + j \quad (17)$$

where Y represents either P_{max}, η or r_q, U_0 is expressed in m/min and P_{arc} in kW.

The coefficients of this law are given in Table 2 for MAG and Hybrid processes. These values have been validated for a welding velocity U_0 from 0.4 m/min to 4 m/min and an arc power P_{arc} from 2 to 11 kW.

4.1. Arc pressure and surface deformation

To better understand the combined effect of both laser beam and electric arc in hybrid laser/MAG welding, numerical models have been developed to study individually the laser and MAG processes. Corresponding experiments have been used to estimate the unknown parameters of the different models. The experiments for

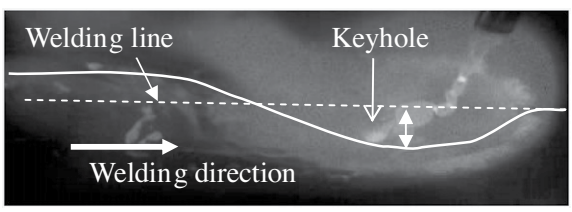

Fig. 3. High speed camera observation of hybrid laser/MAG welding (U_w = 8 m/min – U_0 = 3 m/min) illustrating the measurement of maximal surface deformation.

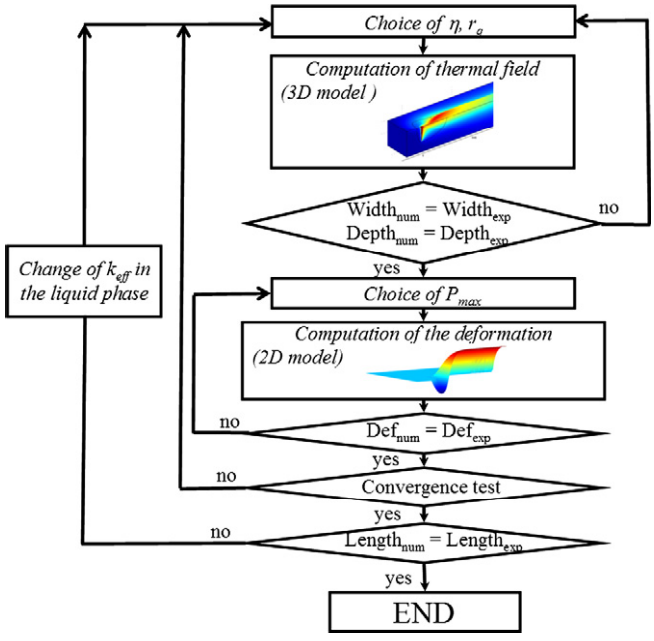

Fig. 4. Schematic diagram of calculated input parameters for the 3D thermal model.

Table 2
Coefficients of the polynomial law Eq. (17) giving the values of P_{max}, η or r_q as a function of welding velocity and arc power for MAG and hybrid processes used in the computations.

	$Y(U_0, P_{surf})$	a	b	c	d	e	f	g	h	i	j	Error (%)
MAG	P_{max} (Pa)	260.2	137.6	−2114.6	−19.7	−141.5	3606.8	1.7	−39.4	636.1	−1886.5	3
	η (%)	−5.4257	−3.824	61.038	−0.3594	12.158	−129.53	0.3666	−7.3102	37.549	47.419	1.5
	r_q (mm)	−0.9296	−0.1066	4.3745	0.0187	0.1644	−6.3446	0.019	−0.4227	2.5565	−0.1879	2.5
Hybrid	P_{max} (Pa)	35.3	−22.4	−169.2	−5.5	172.3	125.3	−11	209.6	−1128	2330.2	2
	η (%)	−2.7767	−0.1626	22.289	−0.4146	7.2754	−79.468	−0.0985	2.6191	−26.054	156.79	7
	r_q (mm)	−0.0186	−0.0039	0.1708	−0.0011	0.05	−0.6518	−0.0033	0.501	−0.1362	1.7915	2.5

the MAG process were conducted with values of wire feeding rates of 3, 5, 9, and 11 m/min (corresponding respectively to an arc power P_{arc} ($U\ I$) of 2336, 3520, 8017, and 10,147 W) and different welding velocities range from 0.6 to 2.4 m/min. For laser experiments, the welding speed varies from 0.5 m/min to 2 m/min. For hybrid welding, the laser beam of 4 kW was located at a distance of 2 mm from the arc axis behind the arc (leading configuration). All these parameters represent 28 different cases. High speed camera observations have shown that, at a wire feeding rate of 3 m/min (I = 146 A), a short-circuiting mode is observed, at 5 m/min (I = 200 A), a globular mode occurs and at higher rates, a spray mode is observed. It can be clearly seen that the surface weld pool deformation due to the action of arc force and droplet impact increases with wire feeding rates and consequently with arc current (Fig. 3). The arc pressure responsible for this deformation has been adjusted in the model in order to get the best fit between calculated and measured values of maximum deformation. For these simulations, the droplet pressure has been ignored. As a result, the arc pressure in our model should be interpreted as a global pressure including the droplet effect as well. The solid line in Fig. 5a shows the estimated arc pressure for the MAG process as a function of current. The comparison between calculated and experimental maximum deformations is presented in Fig. 5b. As expected, the maximum surface deformation increases with the wire feeding rate and consequently with the arc current. At a wire feeding rate of 3 m/min, there is no significant deformation of the weld pool surface. The maximum surface deformation also increases with the welding velocity. It should be mentioned that the values of arc pressure is assumed independent from the welding velocity in the model. The predicted decrease of deformation is induced both by the decrease of the weld pool surface size and the reinforcement surface which depends on the welding velocity.

Fig. 5a compares the values of calculated arc pressure with measurements published by Lin and Eager [28]. In their work, the pressure of gas tungsten welding arcs was measured for currents from 300 to 600 A. Although the processes of GTA and MAG welding are quite different, since in GTA the electrode tip angle is constant whereas in MAG, it continuously varies due to the detachment of droplets, it is interesting to note that the values of arc pressure in the MAG process are close to those observed in the GTA process at 60° or 90° tip angle of the electrode. It should be mentioned that the arc pressure measured by Lin and Eager for GTA was largely used in the past for the numerical simulation of GMA welding without giving any justification or evidence [13,29]. The arc distribution parameter is also consistent with the values for the GTA process given by Kim et al. (extracted from the experimental data of Lin and Eager) [28,29]. The obtained values of arc pressure for hybrid welding are also presented in Fig. 5a. The arc pressure values at currents less than or equal to 200 A (wire feeding rate of 5 m/min) are to be interpreted with caution because of the small values of depression observed at these levels of current. At currents greater than 200 A, the arc pressure obtained for hybrid welding appears to be slightly greater than those observed in the MAG process. This is also confirmed by the values

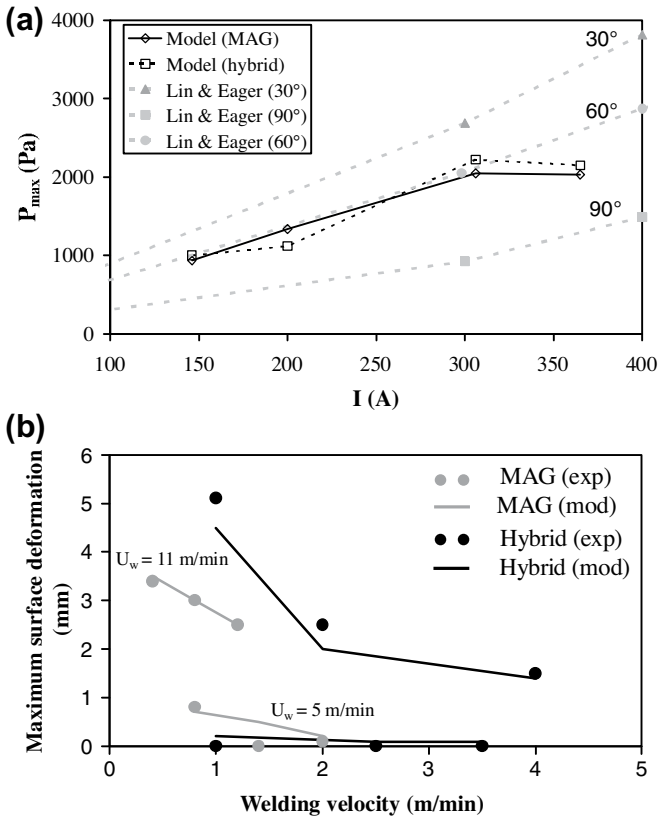

Fig. 5. Calculated arc pressure vs. current for MAG and hybrid welding (a). Comparison with Lin and Eager measurements [28]. Maximum surface deformation comparison between calculation and measurements as a function of welding velocity for MAG and hybrid welding at U_w = 5 m/min and 11 m/min (b).

of deformation (Fig. 5b). These results suggest that the presence of the keyhole influences the value of arc and droplet pressure. However, it was difficult to observe a clear effect of the keyhole from the videos. During hybrid laser-MAG welding, it is possible that the location of impact of the droplets on the weld pool surface differs from that observed in the MAG process. This could modify the equilibrium of the various forces acting on the weld pool surface. Previous works on GMA processes have reported on the mechanisms responsible for droplet formation and detachment, droplet flight in arc plasma and impingement of droplets on the molten pool. Numerical analysis, done for example by Fan, suggests that the electromagnetic force acting on the droplet plays an important role in droplet detachment, in particular at elevated currents [30]. We could imagine that the presence of keyhole and metal vapor ejected from the keyhole have an effect on the physical phenomena in arc plasma, such as heat and fluid flow in gas coupled with electromagnetic forces.

Fig. 6a and b show the calculated longitudinal sections of weld pool geometry of MAG and hybrid processes respectively, at wire

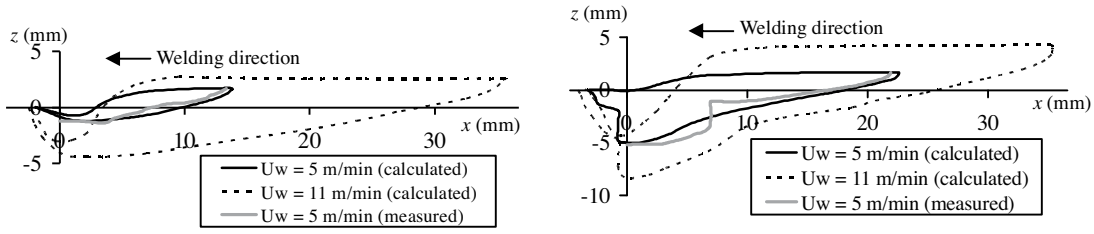

Fig. 6. Predicted longitudinal sections of weld pool geometry in MAG and hybrid processes.

feeding rates of 5 and 11 m/min. The free surface is depressed in the weld pool due to the arc force while the solidified region is elevated owing to the filler metal addition. The pool surface under the arc center is severely deformed while increasing the wire feeding rate. This increase of wire feeding rate causes an increase of current, arc pressure, amount of adding material, and heat coming to the workpiece from the arc and droplets. As a consequence, the weld pool surface will be more deformed, the weld bead will be larger and the solidified weld metal will form pronounced weld reinforcement due to the filler metal addition. Due to the severe deformation of the weld pool, the arc energy is deposited deeper in the material causing greater penetration. In hybrid laser-MAG welding, the shapes of the weld pool differ from those observed in the MAG process due to the presence of the keyhole. The comparison between calculated and experimental longitudinal sections of weld pool geometry is also presented in Fig. 6. For the case of hybrid welding, the measured shape clearly shows a break-up at x = 7 mm, not predicted by the model. The length of the weld pool appears much larger near the surface than near the root. This could be explained by the fluid flow induced by the presence of arc and keyhole. The action of arc is limited to the weld pool surface region. The fluid flow due to arc is primarily driven by surface tension, electromagnetic forces, and gas flow. All these forces act mainly at the weld pool surface. Meanwhile, due to the strong surface depression, the keyhole is located deep inside the workpiece. Its presence will induce fluid motion around the keyhole with a weld pool of limited length. As the model does not take into account these phenomena, the shape of the weld pool can only be predicted approximately.

4.2. Arc efficiency

The computed values of arc efficiency are found to vary between 40% and 70% in MAG and 20%–80% in hybrid laser-MAG welding for all values of current and welding speed investigated (Fig. 7). These numerical values are to be interpreted with caution because of the simplified model used. Indeed the small values of arc efficiency are obtained for elevated currents. However, during welding, a large amount of fumes related to the evaporation of the metal has been observed. As this energy loss is not taken into account in the model, it is necessary to reduce the arc efficiency in the model to predict realistic shapes of weld pools. It should be mentioned that the evaporation heat loss is generally introduced in heat transfer models using the Langmuir equation, as done recently by Zhou and Tsai [11]. However, DebRoy et al. have shown that this equation correlates poorly with the corresponding experimentally determined vaporization rates [31]. They pointed out that the Langmuir equation is valid only at a very low pressure where significant condensation of the vapor does not take place. Experimental data indicate that the vaporization rate under most welding conditions is five to ten times lower than the rate predicted by the Langmuir equation. In the absence of clearly stated

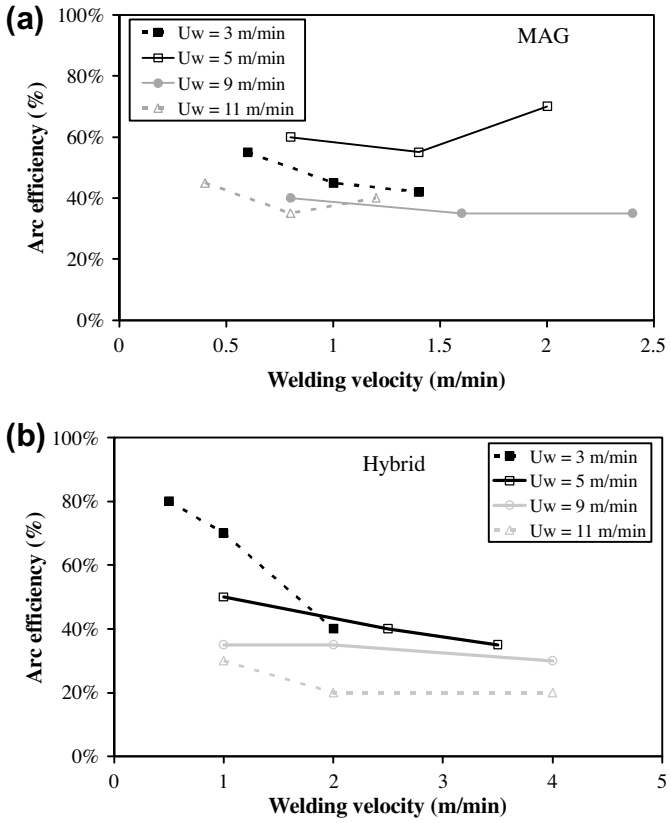

Fig. 7. Arc efficiency as a function of welding velocity at different wire feeding rates for MAG (a) and hybrid (b) processes.

data, the heat loss due to surface evaporation has been ignored in our model.

4.3. Weld pool shapes

The calculated bead shapes for all processes investigated are shown in Fig. 8. The calculated fusion zone geometry for all cases correlates reasonably well with the corresponding experimental results. Furthermore, the solidified weld bead shape and finger penetration could be reasonably predicted by the model. Some discrepancy between the experimental fusion zone geometry and the computed results are observed in Fig. 8a for a wire feeding rate of 9 and 11 m/min in the MAG process. Part of this discrepancy is due to the large surface weld pool deformation observed at elevated currents combined with a large amount of heat coming from droplets. Indeed, the macrograph shows that near the workpiece surface, a wide pool width is produced whereas, deep inside the pool, deep and finger-like penetration is observed. It has been

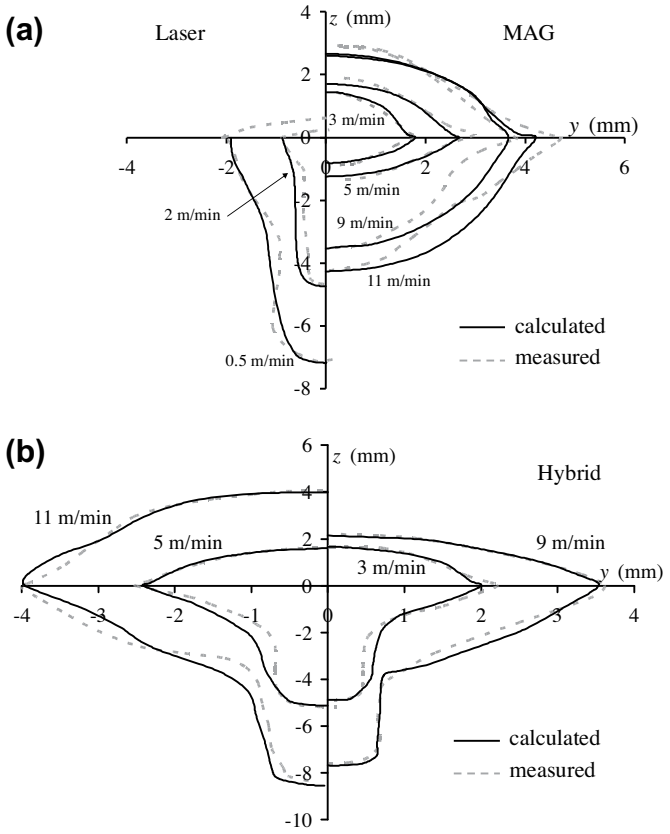

Fig. 8. Transverse cross section of laser and MAG weld (a) at several wire feeding rates and a welding velocity U_0 = 0.8 m/min except for 3 m/min where U_0 = 1 m/min and hybrid weld (U_0 = 1 m/min).

noticed from the high speed camera observations that at elevated currents the arc pressure causes a strong backward flow of the metal. The ejection of the liquid metal at the rear of the arc can even let the base material appear. These specific weld bead shapes cannot be predicted by a purely conductive heat transfer model taking into account only a surface Gaussian heat distribution. For the hybrid laser-MAG welding process, good correlation is observed between calculated and experimental results (Fig. 8b). As expected, the weld bead shape exhibits two zones: a wide bead width near the top surface induced by the arc and a finger-like penetration near the root due to laser action. At a given welding speed (U_0 = 1 m/min), the weld bead size increases with the wire feeding rate, all other parameters are held constant. A deeper penetration is observed indicating a deeper keyhole. This is due to the strong surface weld pool deformation induced by the arc pressure and droplet impact. Thus, the laser hits the surface weld pool at a larger distance from the workpiece top surface.

Fig. 9 shows the comparison between calculated and measured weld pool lengths obtained in laser, MAG, and hybrid processes. To obtain the best fit to experimental results, it was necessary to increase the value of the thermal conductivity of the liquid metal (Table 1). For the case of laser welding, an anisotropic thermal conductivity in the molten material was used with an enhancement factor of 6 (mean value) along the pool length. This can be explained by the strong velocities in the molten material caused by the laser in the welding direction. These results are in accordance with the findings of Safdar who obtained better results with an anisotropic enhanced thermal conductivity with a factor of 5 than with an isotropic one [21]. In the MAG process, an isotropic enhanced conductivity was needed only at high currents, with a

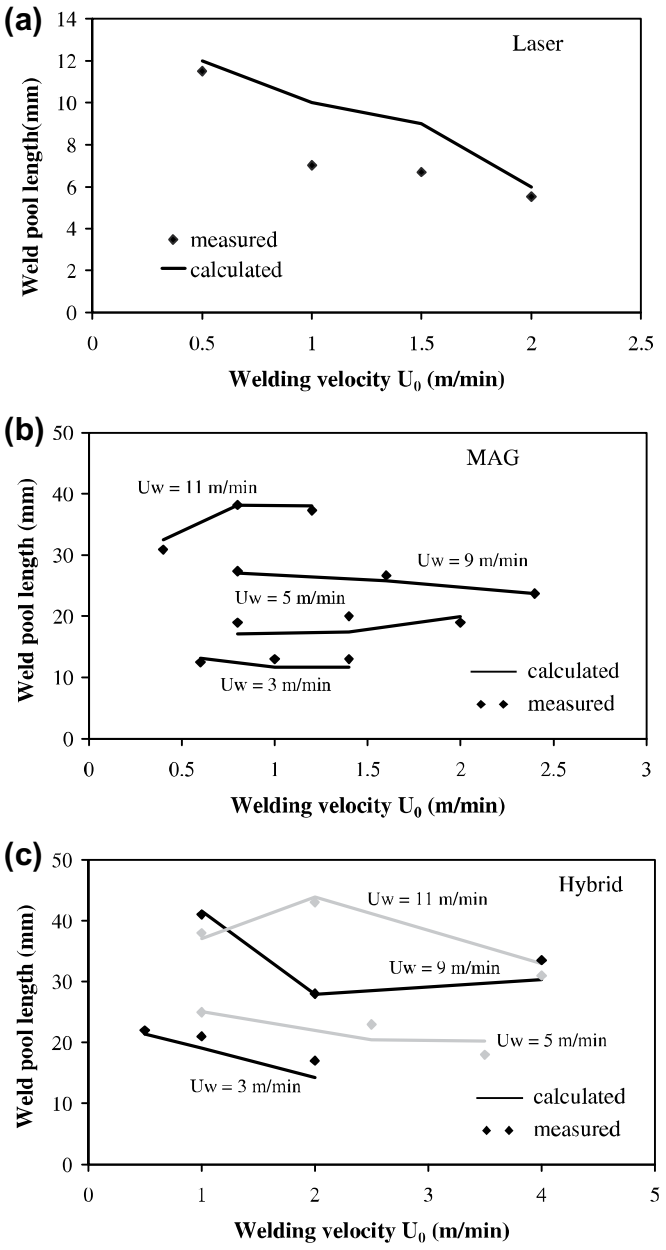

Fig. 9. Calculated and measured weld pool length in laser (a), MAG (b) and hybrid welding (c).

factor of 3. This is probably due to the fluid flow induced by the surface forces, such as Marangoni forces. In that case, the fluid flows radially outwards along the free surface of the molten pool, which tends to widen the weld pool, thus no preponderant direction is observed, contrarily to the case of laser welding. For the case of hybrid laser-MAG welding, the enhanced factor was strongly dependent on the wire feeding rates. At 3 and 5 m/min, an enhancement factor of 6 along the pool length was used, as in laser welding, whereas at 9 and 11 m/min, an isotropic conductivity with an enhancement factor of 3 was used, as in the MAG process. These values suggest that at low currents or wire feeding rates, the pool length observed at the surface is mainly dominated by the laser, whereas at high currents, the MAG has a dominant effect. The results suggest that the weld pool length remains almost constant while welding speed increases, except for laser welding. The weld pool length as observed for other dimensions decreases with

increasing wire feeding rates, since heat input increases with current.

5. Conclusion

In the present study, a 3D quasi-steady state model for heat transfer has been developed to analyze hybrid laser-MAG welding of a S355 steel. Laser and MAG processes were also studied separately. Due to the difficulty in directly measuring some unknowns, limited input parameters were estimated in the model by comparison with experimental data. High speed video camera observations and macrographs were used to obtain transverse and longitudinal cross-sections of welds, weld pool length, and surface weld pool deformation. It was shown that using an appropriate heat source description applied on a deformed weld pool surface, fairly simple and hence computationally efficient models can give reasonable results for a wide range of welding conditions. The major discrepancy between calculated and measured values was observed at high wire feeding rates, corresponding to high arc current welds. It is believed that this effect is caused by the failure of conduction-based models to adequately compensate for convective flow within the pool despite the use of an enhanced thermal conductivity in the molten material. From this numerical analysis combined with an appropriate experimental study, the values of arc pressure, arc efficiency, and maximum surface deformation could be determined from a wide range of welding parameters in MAG and hybrid welding. These values of arc pressure were found to be within the range of values reported in the literature. As for arc efficiency, measurements using calorimeter should be undertaken in the future to confirm the reported values. The values of (η, r_q, P_{max}, k_{eff}) given in the present study can be used as input parameters in other 3D thermal models to simulate hybrid laser/MAG or MAG welding processes of S355 steel in the case of butt-welding. However, in the case of other materials or welding configurations such as T-joint, corresponding experiments need to be conducted to identify the unknown parameters of the model. This simple model could be useful for the simulation of residual stresses and strains in hybrid laser-MAG welding.

Acknowledgments

This study has been realized within the framework of the French National A.N.R. Project "HYPROSOUD". The authors thank Eric Favre and the technical support of Comsol for their useful discussion.

References

[1] M. Ono, Y. Shinbo, A. Yoshitake, M. Ohmura, Development of laser-arc hybrid welding, NKK Tech. Rev. 86 (2002) 8–12.
[2] C. Bagger, F.O. Olsen, Review of laser hybrid welding, J. Laser Appl. 17 (1) (2005) 2–14.
[3] M. Gao, X. Zeng, J. Yan, Q. Hu, Microstructure characteristics of laser-MIG hybrid welded mild steel, Appl. Surf. Sci. 254 (2008) 5715–5721.
[4] M. El Rayes, C. Walz, G. Sepold, The influence of various hybrid welding parameters on bead geometry, Weld. Res. Suppl. Weld. J. (2004) 147–153S.
[5] G. Campana, A. Fortunato, A. Ascari, G. Tani, L. Tomesani, The influence of arc transfer mode in hybrid laser-MIG welding, J. Mater. Process. Technol. 191 (2007) 111–113.
[6] G. Song, L. Liu, P. Wang, Overlap welding of magnesium AZ31B sheets using laser-arc hybrid process, Mater. Sci. Eng. A 429 (2006) 312–319.
[7] R. Fabbro, S. Slimani, F. Coste, F. Briand, Analysis of the various melt pool hydrodynamic regimes observed during CW Nd-YAG deep penetration laser welding, in: Proceedings of ICALEO'2007 Conference, Orlando, USA, Paper No. 802.
[8] M. Wouters, Hybrid Laser-MIG Welding: An Investigation of Geometrical Considerations, Ph.D. Dissertation, Lulea University of Technology, Sweden, 2005.
[9] E.W. Reutzel, S.M. Kelly, R.P. Martukanitz, M.M. Bugarewicz, P. Michaleris, Laser-GMA Hybrid Welding: Process Monitoring and Thermal Modelling, in: S.A. David et al. (Eds.), Proceedings of the 7th International Conference on Trends in Welding Research, Callaway Gardens Resort, Pine Mountain, Georgia, USA, 2005, pp. 143–148.
[10] T. Zhang, C.S. Wu, G.L. Qin, X.Y. Wang, S.Y. Lin, Thermomechanical analysis for laser + GMAW-P hybrid welding process, Comput. Mater. Sci. 47 (2010) 848–856.
[11] J. Zhou, H.L. Tsai, Modeling of transport phenomena in hybrid laser-MIG keyhole welding, Int. J. Heat Mass Transfer 51 (2008) 4353–4366.
[12] J.-H. Cho, S.-J. Na, Three-dimensional analysis of molten pool in GMA-laser hybrid welding, Weld. J. 88 (2009) 35s–43s.
[13] M. Ushio, C.S. Wu, Mathematical modelling of three-dimensional heat and fluid flow in a moving gas metal arc weld pool, Metall. Mater. Trans. B 28B (1997) 509–516.
[14] M. Tanaka, An introduction to physical phenomena in arc welding processes, Weld. Int. 18 (2004) 845–851.
[15] G. Xu, C. Wu, Numerical analysis of weld pool geometry in globular-transfer gas metal arc welding, Mater. Sci. China 1 (2007) 24–29.
[16] G. Xu, J. Hu, H.L. Tsai, Three-dimensional modeling of arc plasma and metal transfer in gas metal arc welding, Int. J. Heat Mass Transfer 52 (2009) 1709–1724.
[17] K.N. Lankalapalli, J.F. Tu, G. Gartner, A model for estimating penetration depth of laser welding processes, J. Phys. D: Appl. Phys. 29 (1996) 1831–1841.
[18] E. Le Guen, Etude du procédé de soudage hybride laser/MAG: caractérisation de la géométrie et de l'hydrodynamique du bain de fusion et développement d'un modèle 3D thermique, Ph.D. Dissertation, Université de Bretagne-Sud, France, 2010.
[19] Données physiques sur quelques aciers d'utilisation courante, Code 15004, Edition OTUA. <www.otua.org/Prop_Physiques/FicheOTUA/OTUA2.html>.
[20] C. Lampa, A.F.H. Kaplan, J. Powell, C. Magnusson, An analytical thermodynamic model of laser welding, J. Phys. D: Appl. Phys. 30 (1997) 1293–1299.
[21] S. Safdar, A.J. Pinkerton, R. Moat, L. Li, M.A. Sheikh, M. Preuss, P.J. Withers, An anisotropic enhanced thermal conductivity approach for modelling laser melt pools, in: ICALEO Conference 2007, Orlando, USA, Paper 1305.
[22] M.A. Wahab, M.J. Painter, M.H. Davies, The prediction of the temperature distribution and weld pool geometry in the gas metal arc welding process, J. Mater. Process. Technol. 77 (1998) 233–239.
[23] A. Kumar, T. DebRoy, Guaranteed fillet weld geometry from heat transfer model and multivariable optimization, Int. J. Heat Mass Transfer 47 (2004) 5793–5806.
[24] D. Gery, H. Long, P. Maropoulos, Effects of welding speed, energy input and heat source distribution on temperature variations in butt joint welding, J. Mater. Process. Technol. 167 (2005) 393–401.
[25] J. Hu, H. Guo, H.L. Tsai, Weld pool dynamics and the formation of ripples in 3D gas metal arc welding, Int. J. Heat Mass Transfer 51 (2008) 2537–2552.
[26] N.S. Tsai, T.W. Eager, Distribution of the heat and current fluxes in gas tungsten arcs, Metall. Trans. B 16B (1985) 841–846.
[27] E. Le Guen, R. Fabbro, M. Carin, F. Coste, P. Le Masson, Analysis of hybrid Nd:Yag laser-MAG arc welding processes, under consideration for publication.
[28] M.L. Lin, T.W. Eager, Pressures produced by gas tungsten arcs, Metall. Trans. B 17B (1986) 601–607.
[29] C.-H. Kim, W. Zhang, T. DebRoy, Modeling of temperature field and solidified surface profile during gas–metal arc fillet welding, J. Appl. Phys. 94 (4) (2003) 2667–2679.
[30] H.G. Fan, R. Kovacevic, A unified model of transport phenomena in gas metal arc welding including electrode, arc plasma and molten pool, J. Phys. D: Appl. Phys. 37 (2004) 2531–2544.
[31] T. DebRoy, S. Basu, K. Mundra, Probing laser induced metal vaporization by gas dynamics and liquid pool transport phenomena, J. Appl. Phys. 70 (3) (1991) 1313–1319.